

ORIGINAL RESEARCH ARTICLE

# Process study for directed energy deposition of 316L stainless steel with TiB<sub>2</sub> metal matrix composites

Yao Ting Ang<sup>1</sup>, Swee Leong Sing<sup>2\*</sup>, Joel Choon Wee Lim<sup>1</sup>

<sup>1</sup>School of Mechanical and Aerospace Engineering, Nanyang Technological University, Singapore

<sup>2</sup>Department of Mechanical Engineering, National University of Singapore, Singapore

## Abstract

In addition to laser powder bed fusion, directed energy deposition (DED) is also gaining interest as an effective metal additive manufacturing technique. Due to its system configuration, it is more efficient and flexible for materials development. Therefore, it can be used for processing of metal matrix composites (MMCs) through the use of powder mixture as feedstock. 316L stainless steel has high corrosion resistance, biocompatibility, and ductility. Several studies have shown the feasibility of using DED to process 316L stainless steel. The material properties of 316L stainless steel can be improved using reinforcement particles such as TiB<sub>2</sub> to form MMCs. In this study, the effects of process parameters on microstructure and mechanical properties of 316L stainless steel reinforced with TiB<sub>2</sub> (316L/TiB<sub>2</sub>) MMC were studied. The process parameters, including laser power, scanning speed, and hopper speed, were varied and analyzed using Taguchi L9 array. It was found that the process parameters have insignificant effect on the bulk density of the samples produced. Through this study, it is also found that tumble mixing was not suitable for the powder feedstock preparation for MMCs to be processed by DED. The microstructure of DED 316L/TiB<sub>2</sub> MMC samples consists of columnar and equiaxed grains. Columnar grains were located within the layers while equiaxed grains were located at the interlayer zones. Fine sub-grains were also observed within these grains and their boundaries were enriched with molybdenum and chromium segregations. Precipitates containing titanium were also observed to segregate at the sub-grain boundaries. Finally, the Vickers microhardness of the DED 316L/TiB<sub>2</sub> MMC was found to be similar to pure 316L stainless steel produced by DED.

**\*Corresponding author:**  
Swee Leong Sing  
(sweeleong.sing@nus.edu.sg)

**Citation:** Ang YT, Sing SL, Lim JCW, 2022, Process study for directed energy deposition of 316L stainless steel with TiB<sub>2</sub> metal matrix composites. *Mater Sci Add Manuf.* 1(2): 13.  
<https://doi.org/10.18063/msam.v1i2.13>

**Received:** April 29, 2022

**Accepted:** June 10, 2022

**Published Online:** June 29, 2022

**Copyright:** © 2022 Author(s). This is an Open Access article distributed under the terms of the Creative Commons Attribution License, permitting distribution, and reproduction in any medium, provided the original work is properly cited.

**Publisher's Note:** Whioce Publishing remains neutral with regard to jurisdictional claims in published maps and institutional affiliations.

**Keywords:** Additive manufacturing; 3D printing; Directed energy deposition; Metal matrix composites; Steels

## 1. Introduction

Additive manufacturing (AM) is a disruptive technology that has gain increasing traction in recent years. AM is a family of techniques and processes that involve the addition of material layer-by-layer with the help of computer-aided designs and computer-aided manufacturing<sup>[1]</sup>. Compared to traditional manufacturing that produces parts by removing material, AM is more flexible and efficient that can reduce manufacturing

costs and environmental impacts<sup>[2]</sup>. AM is also able to create near net shape parts with complex geometries that would otherwise be difficult to manufacture<sup>[3,4]</sup>.

Directed energy deposition (DED) is a popular AM technique for metals that uses a laser beam to melt metal powders onto a substrate. There are various names used for DED, including laser metal deposition, laser cladding, and laser engineered net shaping. One of the key features of DED is its relatively low energy input, resulting in lower residual stresses and smaller heat-affected zones<sup>[5]</sup>. Due to its configuration, DED is ideal for repair and reinforcement cladding applications<sup>[6-8]</sup>. Furthermore, DED is able to create metal matrix composites (MMC) and functionally graded materials that can be customized to meet specific requirements<sup>[9,10]</sup>.

316L stainless steel is one of the most suitable materials for DED. It is a low carbon austenitic steel alloy that has excellent corrosion resistance, ductility, and biocompatibility<sup>[11]</sup>. It is suitable for marine, biomedical, chemical, and even nuclear industry<sup>[12,13]</sup>. However, 316L stainless steel still have relatively low strength, hardness, and wear resistance compared to other alloys such as Ti6Al4V which limits its applications. These shortcomings can be overcome by adding reinforcement particles such as SiC, TiC, and TiB<sub>2</sub> to form MMCs that have significantly higher strength and hardness<sup>[12,14-17]</sup>. Among the various reinforcement particles, TiB<sub>2</sub> is considered one of the most suitable due to its compatibility with 316L stainless steel<sup>[18]</sup>. TiB<sub>2</sub> has high thermal stability, chemical resistance, and wettability with molten steel<sup>[19]</sup>.

One of the main challenges of the DED process is the optimization of the variables involved. The part properties from DED process is highly dependent on these variables such as scanning paths and build part geometry as well as process parameters<sup>[20]</sup>. Variation in these variables will cause a significant change in microstructure and mechanical properties of DED parts. Mukherjee *et al.* observed changes in the thermal distortion of AM parts with process parameters, build geometry, and material<sup>[21]</sup>. Saboori *et al.* also demonstrated that the microstructure and tensile strength of 316L stainless steel cuboids created by DED varied depending on the deposition strategy due to the differences in cooling rate<sup>[22]</sup>.

There have been some studies on the effects of variables on MMCs using 316L stainless steel as the matrix. Ertugrul *et al.* showed that using proper powder preparation, the addition of TiC particles increased the hardness by about 100 HV as compared to pure 316L stainless steel<sup>[14]</sup>. Wu *et al.* showed that increasing the SiC content in 316L stainless steel MMCs would result in higher hardness but lower corrosion resistance<sup>[12]</sup>. Other researchers such as

AlMangour *et al.* were able to find that for laser powder bed fusion (L-PBF), which is another type of metal AM technique, 316L with 10 vol.% TiB<sub>2</sub> was optimum to produce finer microstructure and better mechanical properties<sup>[18]</sup>. They attributed the improvement in mechanical properties to Orowan and grain boundary strengthening. However, there is currently no known research on the process parameter optimization of 316L stainless steel reinforced with TiB<sub>2</sub> particles for DED. Optimizations of these process parameters are crucial to produce parts with desired mechanical properties with minimal defects, thus, increasing the flexibility and usage of DED for a wider range of applications.

In this study, an optimal set of process parameters for 316L stainless steel with TiB<sub>2</sub> MMC (316L/TiB<sub>2</sub>) was determined. The effects of process parameters on the mechanical properties and microstructure of 316L/TiB<sub>2</sub> were evaluated. The Taguchi L9 array was used to design the experiments and to optimize the process parameters for optimum mechanical properties. The three process parameters varied were laser power, scanning speed, and hopper speed at three different levels. Pre-mixed 316L stainless steel with 6 wt.% TiB<sub>2</sub> powder was used and other parameters such as laser spot size and scanning strategy were kept constant. Optical microscopy and scanning electron microscopy (SEM) were used to evaluate the microstructure of the samples. Finally, the density and Vickers hardness of the samples were also determined and discussed.

## 2. Materials and methods

### 2.1. Powder preparation

Gas atomized 316L stainless steel powder with particle size distribution 40–100 μm from TLS Technik (Germany) was tumble mixed with 6 wt.% TiB<sub>2</sub> nanoparticles. The powder mixture was mixed for 8 h at 60 rpm using the Inversina 2L Tumbler Mixer (Bioengineering AG, Switzerland). The chemical composition of the 316L stainless steel powder is listed in Table 1.

The powders before and after mixing were examined using SEM to ensure that the TiB<sub>2</sub> particles adhere to the 316L stainless steel particles and are homogeneously dispersed. TiB<sub>2</sub> particles were observed to be evenly coated and distributed on the 316L stainless steel particles. The

**Table 1. Chemical composition of 316L stainless steel powder**

Material	Chemical composition (wt.%)								
	C	Mn	P	S	Si	Cr	Ni	Mo	Fe
316L	0.03	2	0.045	0.03	1	16-18	10-14	2-3	Bal.

SEM images of the 316L stainless steel and TiB<sub>2</sub> powder before and after mixing are shown in Figure 1.

2.2. DED

The fabrications were conducted using a DMG Mori LASERTEC 65 3D (Germany). The laser unit consists of a 2.5 kW diode-pumped laser that has 3 mm laser spot size and produce wavelengths ranging from 900 nm to 1080 nm. The powder focus distance used is 11 mm and the argon gas flow rate for shielding was 6 l/min. The fixed parameters used for the fabrication are shown in Table 2.

To optimize the process parameters, a L9 Taguchi array was used that varied laser power, scanning speed, and hopper speed at three levels. The Taguchi L9 array and the parameters used are tabulated in Table 3. The energy density,  $\epsilon$ , is calculated using the following equation:

$$\epsilon = \frac{P}{v \times d}$$

where  $P$  is the laser power (W),  $v$  is the scanning speed (mm/min), and  $d$  is the laser spot size (mm).

The range of each parameter was obtained by preliminary experiments that vary the parameters for single clad. For example, at 600 W laser power, very little material was deposited while at 1800 W laser power, overheating was observed. The parameter ranges were also chosen such that the energy density for all the Taguchi runs is between the known optimal DED process parameters for pure 316L stainless steel and its composites. Due to formation of powder clouds during the DED process, which is attributed to the presence of TiB<sub>2</sub> particles, the powder flow rate could not be accurately measured; hence, hopper speed was varied instead.

For each set of Taguchi parameters, three 20 mm × 20 mm × 10 mm cuboids were fabricated on 304 stainless steel substrates. Each of the three cuboids was built concurrently, layer-by-layer, in a zig-zag path as shown in Figure 2.

The DED produced cuboids were then separated from the substrate using wire electrical discharge machining. The samples were cut 1 mm above the substrate such that the samples analyzed are not contaminated with the substrate material due to dilution effect.

The results obtained from the experiments were converted into a signal-to-noise (S/N) ratio. The S/N ratio converts the results into a logarithmic scale to account for non-linear relationships. It is also robust as it considers both the mean and variance of the results. The “larger is better” S/N ratio approach was used and the formula for S/N ratio is given by:

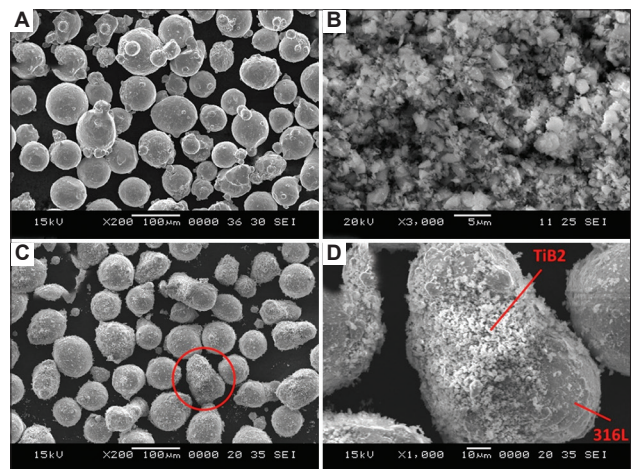


Figure 1. Scanning electron microscopy images: (A) pure 316L stainless steel powder, (B) TiB<sub>2</sub> nanoparticles, (C) mixed 316L/TiB<sub>2</sub> powder mixture, and (D) higher magnification showing TiB<sub>2</sub> particles adhering to surface of a 316L stainless steel particle.

Table 2. Fixed process parameters for DED

Fixed process parameters	Values
Spot size	3 mm
Powder focus	11 mm
Shield gas	Argon
Gas flow rate	6 l/min
Overlap rate	50%
Layer step height	1 mm
Scanning pattern	Zig-zag

$$S/N = -10 \log_{10} \frac{\sum_{i=1}^n \frac{1}{y_i^2}}{n} \tag{1}$$

Where  $y_i$  is the raw measurement value and  $n$  is the number of measurements for each Taguchi parameter.

2.3. Microstructure analysis

The DED samples were ground using 320 grit sandpaper, followed by polishing using 9 μm, 3 μm, 1 μm diamond suspension, and 0.25 μm standard fumed silica suspension (OP-S). Samples were rinsed with water after each step.

The polished samples were first observed using an Olympus SZX7 (Japan) optical microscope to check for pores and cracks. The samples were then etched by swabbing the surfaces with Marble’s Reagent for 10 s. The microstructure was then observed using JEOL 5600LV (United States) SEM. Energy dispersive X-ray spectroscopy (EDS) was also used to identify the compositions of the microstructures found using the same equipment as the SEM.

Table 3. I9 Taguchi array with estimated powder flow rate and energy density

Taguchi Number	Run Order	Laser power (W)	Scanning speed (mm/min)	Hopper speed (rpm)	Estimated powder rate (g/min)	Energy density (J/mm <sup>2</sup> )
1	1	1000	200	200	5.44	100.0
2	2	1000	400	300	7.85	50.0
3	3	1000	600	400	9.95	33.3
4	8	1200	200	300	7.85	120.0
5	9	1200	400	400	9.95	60.0
6	7	1200	600	200	5.44	40.0
7	6	1400	200	400	9.95	140.0
8	4	1400	400	200	5.44	70.0
9	5	1400	600	300	7.85	46.7

**2.4. Density measurements**

The method of hydrostatic weighing was used to measure the bulk density of the polished samples based on Archimedes’ Principle. The XS204 balance machine with density kit (Mettler Toledo, Switzerland) was used to perform the density tests.

The actual TiB<sub>2</sub> content of the DED samples was calculated using the rule of mixture:

$$f = \frac{\frac{1}{\rho} - \frac{1}{\rho_s}}{\frac{1}{\rho_T} - \frac{1}{\rho_s}} \tag{2}$$

Where *f* is the weight fraction of TiB<sub>2</sub>, *P<sub>s</sub>* and *P<sub>T</sub>* are the density of 316L stainless steel (8.00 g/cm<sup>3</sup>) and TiB<sub>2</sub> (4.52 g/cm<sup>3</sup>), respectively. The calculated TiB<sub>2</sub> weight fraction assumes that the DED samples have no porosity.

**2.5. Microhardness**

The Vickers hardness of the polished samples was measured using FM-300e hardness tester (Micro Measurement Pte Ltd, Singapore) at a load of 300 g for 15 s, according to ISO 6507-1:2018. Six evenly spaced indentations were made on both the top and side surfaces.

**3. Results and discussion**

**3.1. Microstructure**

The optical micrographs of the polished side and top surfaces with clear boundaries between the melt pools are shown in Figure 3.

The melt pool boundaries were formed during the remelting of layers and adjacent scan tracks when subsequent powder is deposited following the scanning

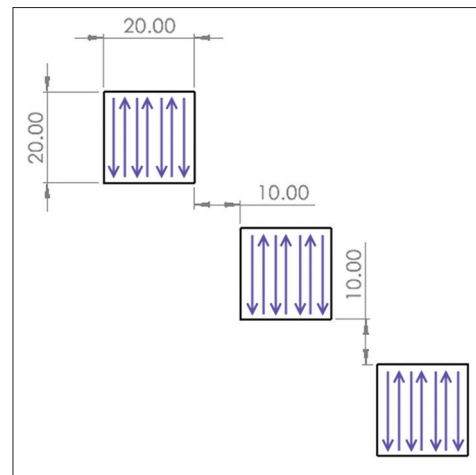


Figure 2. Scanning path used in directed energy deposition.

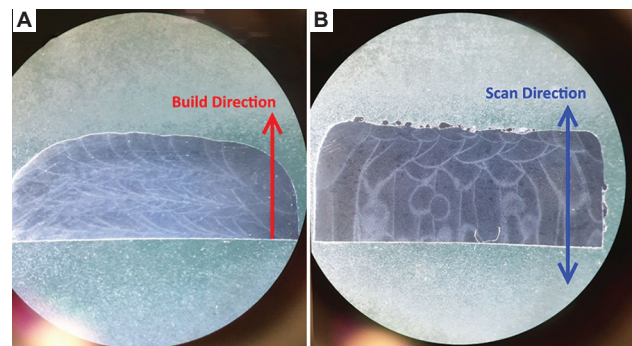


Figure 3. Optical micrographs: (A) side surface and (B) top surface with melt pool boundaries.

path. As seen in Figure 3B, the scan tracks formed straight lines following the scanning path but stops abruptly near the edge of the sample. This is due to the laser momentarily turning off and on as it shifts to the adjacent linear path, remelting and forming a separate melt pool during the DED process. No crack or visible pore can be observed in

all the DED samples. The optical micrographs using higher magnifications are shown in Figure 4.

Precipitates between 1 μm and 2 μm were identified to be TiB<sub>2</sub> within the 316L stainless steel matrix, which can be a result of agglomeration of the particles. Further magnifications also revealed finer precipitates that were smaller than 1 μm. These nanoinclusions are not pores and were identified by Saeidi *et al.* to be silicate-chromium phases<sup>[23]</sup>. Due to the low wettability of silicon with steel, it tends to separate from the melt pools during the DED process. It is also circular to reduce surface tension due to the high viscosity of the silicate melt. These nanoinclusions could also be TiB<sub>2</sub> due to their similarity in size. The SEM images of the polished and etched top and side surfaces reveal the microstructure of DED 316L/TiB<sub>2</sub> MMC as shown in Figure 5.

The microstructure mainly consists of epitaxial columnar grains that grow along the build direction. This is because the previously deposited layers act as a heat sink

and affect the direction of heat flow, resulting in a vertical temperature that encouraged columnar grains to grow<sup>[24]</sup>. At the interlayer zone, the microstructure morphology is made of fine equiaxed grains that were formed during remelting when a subsequent layer is deposited on top of it. The high cooling rates during the deposition of subsequent layers result in equiaxed grain growth. It is well documented that the difference solidification microstructure formed is due to the thermal gradients and cooling rate<sup>[23-25]</sup>.

Within each of the columnar and equiaxed grains, there exist complex and intricate sub-grains. These sub-grains are not actual grains but were formed due to the segregation of the alloying molybdenum during the rapid solidification process<sup>[23]</sup>. There is insufficient time for the heavier molybdenum to dissolve into the matrix during solidification, leading to the enrichment of molybdenum at the sub-grain boundaries. The sub-grain boundaries are more chemically resistant than the matrix as revealed during the etching process. They also have high dislocation concentrations and help to strengthen the DED samples. Tan *et al.* were able to relate the Vickers hardness of DED 316L stainless steel to the sizes of these sub-grains using the Hall-Petch relationship<sup>[24]</sup>. The molybdenum enrichment at the sub-grain boundaries is confirmed using EDS for both equiaxed and columnar grains, as shown in Table 4. The locations for EDS are shown in Figure 6.

There is an enrichment of molybdenum and chromium with depletion of iron in the sub-grain boundaries compared to the matrix for both equiaxed and columnar grains. This agrees with the results obtained for pure 316L stainless steel<sup>[24]</sup>. EDS analysis of some of the larger precipitates showed presence of titanium, which confirmed that TiB<sub>2</sub> was successfully deposited during the DED process. Element mapping for titanium (Figure 7) shows high concentration of titanium that coincided with the location of precipitates. These precipitates are located the sub-grain boundaries and suggest that the actual TiB<sub>2</sub>

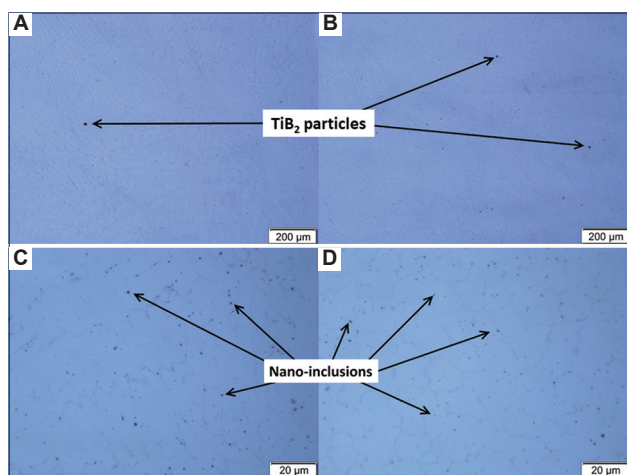


Figure 4. Optical micrographs of unetched samples at ×5 magnification for (A) side surface and (B) top surface and at ×50 magnification for (C) side surface and (D) top surface.

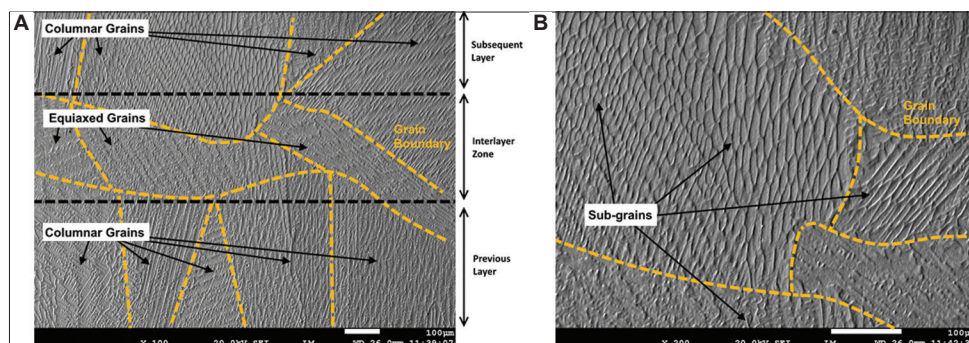


Figure 5. Scanning electron microscopy image of side surface (A) showing columnar and equiaxed grains and (B) higher magnification showing the sub-grains in the columnar and equiaxed grains.

content in the MMC samples may be significantly lower than 2 wt.%. This may account for the negligible differences in the results obtained for 316L/TiB<sub>2</sub> MMC as compared to pure 316L stainless steel.

### 3.2. Density

The mean and S/N ratio of the measured density is tabulated in Table 5, with the calculated weight fraction of TiB<sub>2</sub> in the DED samples. The average weight fraction of TiB<sub>2</sub> is 2 wt.% which is significantly lower than the added

weight fraction of 6 wt.%. This indicates that the powder clouds formed during the DED process can be the TiB<sub>2</sub> particles that escaped during the powder deposition.

Even though TiB<sub>2</sub> particles were observed to be adhering onto the 316L stainless steel particle surfaces, the tumble mixing process did not induce sufficient adhesion which caused the TiB<sub>2</sub> particles to separate from the 316L stainless steel particles during powder deposition. The powder deposition step involves forces induced by the gas flow to expulse the powder from the nozzle. Tumble mixing is not suitable for mixing nanoparticle composites for DED as the process involves injecting the mixed powder into a fast-moving gas stream. Larger TiB<sub>2</sub> particles can also be used as they are less likely to escape due to higher gravitational force acting on them. Ball milling can be used to strengthen the adhesion during the mixing<sup>[18]</sup>. During ball milling, mechanical alloying is achieved due to the repeated deformation, fracturing, and cold welding of the powder particles<sup>[18,26]</sup>. At the start, the reinforcement particles fracture due to their brittleness before sticking onto the matrix powder in which cold welding predominates due to plastic deformation. During the deformation and cold welding of the matrix powder particles, the reinforcement particles then dispersed inside the matrix. Fracture then takes over due to the matrix hardening. Finally, a dynamic balance between cold welding and fracture ensures the absence of agglomeration<sup>[27]</sup>. In addition, the collisions can cause the break-up of agglomerated particles<sup>[18]</sup>. However, it is of interest to note that using larger particles or ball milling result in a morphological change to the powder, which, in turn, may affect the powder flowability. Hence, a careful control of the powder preparation parameters is needed. With controlled parameters used during the process, the centrifugal effect of ball milling results in uniform dispersion of the reinforcement particles in the powder mixture with minimum change in powder morphology. It has been found that mechanical alloying

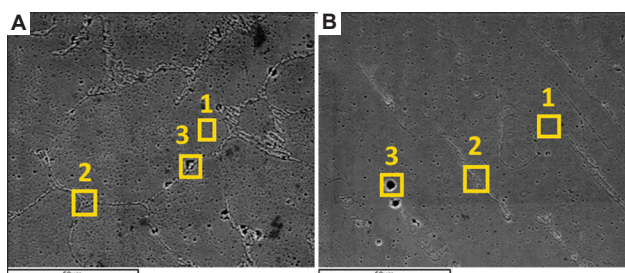


Figure 6. Energy dispersive X-ray spectroscopy locations for (A) equiaxed and (B) columnar grains. Location 1 is within the matrix, location 2 is at the sub-grain boundary, and location 3 is at the TiB<sub>2</sub> particle.

Table 4. Composition for equiaxed and columnar grains

Element	Equiaxed (wt.%)			Columnar (wt.%)		
	Matrix	Boundary	TiB <sub>2</sub>	Matrix	Boundary	TiB <sub>2</sub>
S	1.06	-	1.6	0.48	-	-
Cr	16.48	22.27	19.18	16.26	21.86	22.75
Mn	1.38	1.83	-	1.33	1.8	2.6
Fe	67.69	54.09	66.34	69.81	62.03	46.25
Ni	10.13	6.38	9.03	10.66	9.3	3.86
Ti	-	-	3.85	-	-	5.57
Mo	-	10.69	-	-	5.01	4.4
Others	3.26	4.74	-	1.46	-	14.57
Total	100	100	100	100	100	100

Table 5. Mean, S/N ratio of sample density, and calculated weight fraction of TiB<sub>2</sub>

Taguchi number	Laser power (W)	Scanning speed (mm/min)	Hopper speed (rpm)	Mean density (g/cm <sup>3</sup> )	S/N	f
1	1000	200	200	7.891±0.004	17.943	1.8%
2	1000	400	300	7.879±0.011	17.929	2.0%
3	1000	600	400	7.874±0.016	17.924	2.1%
4	1200	200	300	7.887±0.002	17.938	1.9%
5	1200	400	400	7.876±0.002	17.926	2.0%
6	1200	600	200	7.855±0.012	17.903	2.4%
7	1400	200	400	7.876±0.003	17.927	2.0%
8	1400	400	200	7.883±0.006	17.934	1.9%
9	1400	600	300	7.862±0.008	17.910	2.3%

improves the distribution of Si<sub>3</sub>N<sub>4</sub> and AlN in Al6061 aluminum powder. While the process also decreases the reinforcement particle size, it improved the composite characteristics by eliminating the reinforcement particle defects. Furthermore, the mechanical alloying also improved the matrix characteristics due to deformation and dislocations<sup>[28]</sup>. During mechanical alloying, it is possible for the morphology of powders to change from spherical to flattened and finally to nearly spherical again<sup>[29]</sup>. It was also observed that while the particle size of the mixed powder decreases with increase in milling time, there is a limit after which, the particle size will remain stable due to equilibrium between the cold welding and repeated fracture<sup>[30-32]</sup>. Hence, it is important to investigate

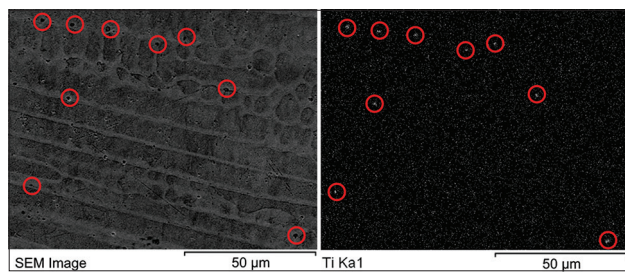


Figure 7. Energy dispersive X-ray spectroscopy element mapping for titanium. Red circles demarcate areas of high titanium concentrations, which coincide with the location of precipitates seen in the scanning electron microscopy image.

Table 6. Response for density

Level	Laser power	Scanning speed	Hopper speed
1	17.932	17.936	17.927
2	17.922	17.930	17.926
3	17.924	17.912	17.926
Delta	0.0097	0.0235	0.0009
Rank	2	1	3

Table 7. Mean and S/N ratio of hardness

Taguchi Number	Laser Power W	Scanning Speed mm/min	Hopper Speed rpm	Mean Hardness HV	S/N
1	1000	200	200	183.5±8.5	45.244
2	1000	400	300	178.7±9.8	45.006
3	1000	600	400	186.0±8.4	45.367
4	1200	200	300	173.9±10.4	44.762
5	1200	400	400	186.4±5.1	45.399
6	1200	600	200	181.1±5.0	45.151
7	1400	200	400	181.9±9.9	45.161
8	1400	400	200	168.5±5.5	44.519
9	1400	600	300	177.6±6.1	44.977

and determine the optimum process conditions for powder mixing.

The effect of each variable on the density of the DED samples is shown in Figure 8. Table 6 shows the ranks and deltas of the S/N ratios. The delta is the difference between the highest and lowest average response for each variable.

It was found that the variation of density was not significant across the various parameters and that the effect of each of the variable was negligible on the density of the DED 316/TiB<sub>2</sub> MMC. The spread of mean density across the DED samples was <0.5% and the delta is <0.1 for all three variables. However, the DED samples were still denser compared to same material produced using sintering and L-PBF<sup>[33]</sup>. Furthermore, no visible pore or crack was observed in the samples.

### 3.3. Microhardness

The mean and S/N ratio of the measured Vickers hardness of the DED samples are shown in Table 7. The mean microhardness varied between 168.5 HV and 186.4 HV, which is similar to pure 316L samples produced by DED<sup>[34]</sup>.

The addition of TiB<sub>2</sub> did not increase the hardness as compared to DED produced 316L stainless steel. This may be due to the low actual content of TiB<sub>2</sub> in the obtained DED samples. AlMangour *et al.* found that there is a critical weight fraction of TiB<sub>2</sub> between 3 wt.% and 6 wt.% that would significantly increase the hardness values of 316L/TiB<sub>2</sub> MMC produced by L-PBF<sup>[33]</sup>. In addition, Du *et al.* obtained 316/TiB<sub>2</sub> MMC with up to 900 HV using 20 wt.% TiB<sub>2</sub><sup>[15]</sup>. Hence, the TiB<sub>2</sub> content in the DED samples must be increased to achieve higher hardness.

The effect of each variable on the microhardness of DED samples is shown in Figure 9. Table 8 shows the ranks and deltas of the S/N ratio for hardness.

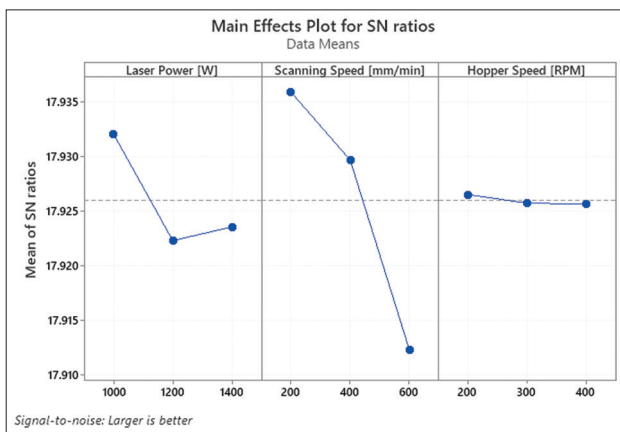


Figure 8. Main effect graph for sample density.

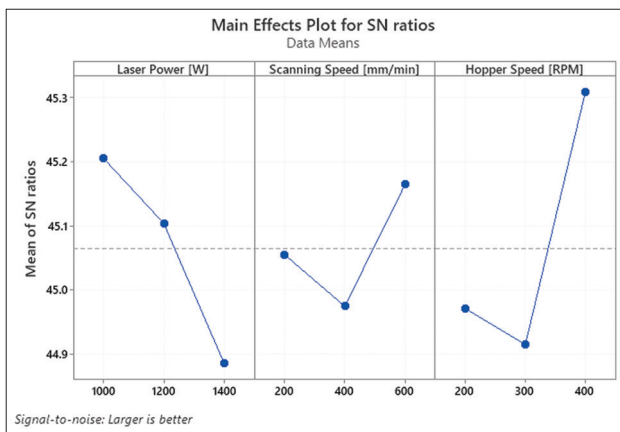


Figure 9. Main effects graph for microhardness.

Table 8. Response for microhardness

Level	Laser power	Scanning speed	Hopper speed
1	45.21	45.06	44.97
2	45.10	44.97	44.92
3	44.89	45.16	45.31
Delta	0.32	0.19	0.39
Rank	2	3	1

Hopper speed was found to be the most influential in affecting the microhardness of the DED 316L/TiB<sub>2</sub> MMC, followed by laser power and scanning speed. The optimum parameters for maximum hardness were found to be laser power of 1000 W, scanning speed of 600 mm/min, and hopper speed of 400 rpm. This gives a predicted microhardness of 182.5 HV. As these optimum parameters are identical to Taguchi No. 3, there is no confirmation run conducted. The experimental value of microhardness obtained from this run is 186.0 HV which means the predicted value has a 1.9 % error which showed

the accuracy of the prediction. The Taguchi method was effective in determining the optimal set of parameters for DED 316L/TiB<sub>2</sub> MMC.

#### 4. Conclusions

In this study, 316L/TiB<sub>2</sub> MMC was successfully fabricated using DED. The effect of DED process parameters on the microstructure and mechanical properties of 316L/TiB<sub>2</sub> MMC was studied. The L9 Taguchi array was used to vary laser power, scanning speed, and hopper speed at three levels to optimize the mechanical properties of 316L/TiB<sub>2</sub>.

It was found that the laser power, scanning speed, and hopper speed had negligible effects on the density of the samples produced. Although 6 wt.% of TiB<sub>2</sub> is added, the average weight fraction of TiB<sub>2</sub> in DED 316L/TiB<sub>2</sub> was calculated to be 2 wt.%, indicating loss of TiB<sub>2</sub> during the DED process. Tumble mixing was found to be unsuitable for the preparation of powder mixture feedstock for DED as it does not result in sufficient adhesion between the TiB<sub>2</sub> and 316L stainless steel particles. No pore and crack were observed in all the DED samples. Columnar grains were found predominantly within the layers while equiaxed grains were found at the interlayer zones for the DED samples. Fine and intricate sub-grains were also observed within the grains. EDS analysis showed that the sub-grain boundaries are enriched with molybdenum and chromium. The microhardness of DED 316L/TiB<sub>2</sub> MMC ranged between 168.5 HV and 186.4 HV.

In the future, effect of different powder preparation methods for 316L/TiB<sub>2</sub> can be studied to improve the efficiency of the process. Then, the different compositions of MMC can be investigated to expand the material library available for the DED process.

#### Acknowledgments

The authors acknowledge the support from National Additive Manufacturing Innovation Cluster (NAMIC), Singapore, for the use of the AM facilities.

#### Funding

S. L. Sing would like to acknowledge the funding support from Singapore Ministry of Education Academic Research Fund Tier 1 (Award No.: 22-3721-A0001).

#### Conflict of interest

The authors declared no potential conflict of interest with respect to the research, authorship, and/or publication of this article.

## Author contributions

*Conceptualization:* Swee Leong Sing

*Formal analysis:* Yao Ting Ang

*Investigation:* Joel Choon Wee Lim, Yao Ting Ang

*Methodology:* Swee Leong Sing, Yao Ting Ang

*Project administration:* Swee Leong Sing

*Resources:* Swee Leong Sing

*Supervision:* Swee Leong Sing

*Validation:* Joel Choon Wee Lim, Yao Ting Ang

*Visualization:* Swee Leong Sing, Yao Ting Ang

*Writing–original draft:* Swee Leong Sing, Yao Ting Ang

*Writing–review and editing:* Swee Leong Sing.

## References

1. Herzog D, Seyda V, Wycisk E, *et al.*, 2016, Additive manufacturing of metals. *Acta Mater*, 117: 371–392.  
<https://doi.org/10.1016/j.actamat.2016.07.019>
2. Frazier W, 2014, Metal additive manufacturing: A review. *J Mater Eng Perform*, 23: 1917–1928.
3. Michel F, Lockett H, Ding J, *et al.*, 2018, A modular path planning solution for Wire + Arc additive manufacturing. *Robot Comput Integr Manuf*, 60: 1–11.  
<https://doi.org/10.1016/j.rcim.2019.05.009>
4. Ding D, Pan Z, Cuiuri D, *et al.*, 2016, Adaptive path planning for wire-feed additive manufacturing using medial axis transformation. *J Cleaner Prod*, 133: 942–952.  
<https://doi.org/10.1016/j.jclepro.2016.06.036>
5. Feenstra DR, Cruz V, Gao X, *et al.*, 2020, Effect of build height on the properties of large format stainless steel 316L fabricated via directed energy deposition. *Addit Manuf*, 34: 101205.  
<https://doi.org/10.1016/j.addma.2020.101205>
6. Saboori A, Aversa A, Marchese G, *et al.*, 2019, Application of directed energy deposition-based additive manufacturing in repair. *Appl Sci*, 9: 3316.  
<https://doi.org/10.3390/app9163316>
7. Dass A, Moridi A, 2019, State of the art in directed energy deposition: From additive manufacturing to materials design. *Coatings*, 9: 418.  
<https://doi.org/10.3390/coatings9070418>
8. Dharmawan AG, Soh GS, 2022, A cylindrical path planning approach for additive manufacturing of revolved components. *Mater Sci Addit Manuf*, 1: 3.  
<https://doi.org/10.18063/msam.v1i1.3>
9. Ansari M, Jabari E, Toyserkani E, 2021, Opportunities and challenges in additive manufacturing of functionally graded metallic materials via powder-fed laser directed energy deposition: A review. *J Mater Porc Technol*, 294: 117117.  
<https://doi.org/10.1016/j.jmatprotec.2021.117117>
10. Groden C, Traxel KD, Afrouzian A, *et al.*, 2022, Inconel 718-W7Ni3Fe bimetallic structures using directed energy deposition-based additive manufacturing. *Virtual Phys Prototyp*, 17: 170–180.  
<https://doi.org/10.1080/17452759.2022.2025673>
11. Sehhat MH, Sutton AT, Hung CH, *et al.*, 2022, Plasma spheroidization of gas-atomized 304L stainless steel powder for laser powder bed fusion process. *Mater Sci Addit Manuf*, 1: 11.  
<https://doi.org/10.18063/msam.v1i1.1>
12. Wu CL, Zhang S, Zhang CH, *et al.*, 2019, Effects of SiC content on phase evolution and corrosion behavior of SiC-reinforced 316L stainless steel matrix composites by laser melting deposition. *Optics Laser Technol*, 115: 134–139.  
<https://doi.org/10.1016/j.optlastec.2019.02.029>
13. Fu C, Li J, Bai J, *et al.*, 2021, Effect of helium bubbles on irradiation hardening of additive manufacturing 316L stainless steel under high temperature He ions irradiation. *J Nucl Mater*, 550: 152948.  
<https://doi.org/10.1016/j.jnucmat.2021.152948>
14. Ertugrul O, Enrici TM, Paydas H, *et al.*, 2020, Laser cladding of TiC reinforced 316L stainless steel composites: Feedstock powder preparation and microstructural evaluation. *Powder Technol*, 375: 384–396.  
<https://doi.org/10.1016/j.powtec.2020.07.100>
15. Du B, Zou Z, Wang X, *et al.*, 2008, Laser cladding of in situ TiB<sub>2</sub>/Fe composite coating on steel. *Appl Surf Sci*, 254: 6489–6494.  
<https://doi.org/10.1016/j.apsusc.2008.04.051>
16. Koh HK, Moo JG, Sing SL, *et al.*, 2022, Use of fumed silica nanostructured additives in selective laser melting and fabrication of steel matrix nanocomposites. *Materials*, 15: 1869.  
<https://doi.org/10.3390/ma15051869>
17. Chen W, Xu L, Zhang Y, *et al.*, 2022, Additive manufacturing of high-performance 15-5PH stainless steel matrix composites. *Virtual Phys Prototyp*, 17: 366–381.  
<https://doi.org/10.1080/17452759.2021.2019793>
18. AlMangour B, Grzesiak D, Yang JM, 2017, Selective laser melting of TiB<sub>2</sub>/316L stainless steel composites: The roles of powder preparation and hot isostatic pressing post-treatment. *Powder Technol*, 309: 37–48.  
<https://doi.org/10.1016/j.powtec.2016.12.073>
19. AlMangour B, Kim YK, Grzesiak D, *et al.*, 2019, Novel TiB<sub>2</sub>-reinforced 316L stainless steel nanocomposites with excellent room and high-temperature yield strength developed by additive manufacturing. *Compos Part B Eng*,

- 156: 51–63.  
<https://doi.org/10.1016/j.compositesb.2018.07.050>
20. Lu X, Chiumenti M, Cervera M, *et al.*, 2021, Substrate design to minimize residual stresses in directed energy deposition AM processes. *Mater Des*, 202: 109525.  
<https://doi.org/10.1016/j.matdes.2021.109525>
21. Mukherjee T, Manvatkar V, De A, DebRoy T, 2017, Mitigation of thermal distortion during additive manufacturing. *Script Mater*, 127: 79–83.  
<https://doi.org/10.1016/j.scriptamat.2016.09.001>
22. Saboori A, Piscopo G, Lai M, *et al.*, 2020, An investigation on the effect of deposition pattern on the microstructure, mechanical properties and residual stress of 316L produced by directed energy deposition. *Mater Sci Eng A*, 780: 139179.  
<https://doi.org/10.1016/j.msea.2020.139179>
23. Saeidi K, Gao X, Zhong Y, *et al.*, 2015, Hardened austenite steel with columnar sub-grain structure formed by laser melting. *Mater Sci Eng A*, 625: 221–229.  
<https://doi.org/10.1016/j.msea.2014.12.018>
24. Tan ZE, Pang JH, Kaminski, *et al.*, 2019, Characterisation of porosity, density, and microstructure of directed energy deposited stainless steel AISI 316L. *Addit Manuf*, 25: 286–296.  
<https://doi.org/10.1016/j.addma.2018.11.014>
25. Yadroitsev I, Krakhmalev P, Yadroitsava I, *et al.*, 2013, Energy input effect on morphology and microstructure of selective laser melting single track from metallic powder. *J Mater Proc Technol*, 213: 600–613.  
<https://doi.org/10.1016/j.jmatprotec.2012.11.014>
26. Zhang DL, 2004, Processing of advanced materials using high-energy mechanical milling. *Prog Mater Sci*, 49: 537–560.
27. Suryanarayana C, Ivanov E, Boldyrev VV, 2002, The science and technology of mechanical alloying. *Mater Sci Eng A*, 304–306: 151–158.  
[https://doi.org/10.1016/s0921-5093\(00\)01465-9](https://doi.org/10.1016/s0921-5093(00)01465-9)
28. Fogagnolo JB, Velasco F, Robert MH, *et al.*, 2003, Effect of mechanical alloying on the morphology, microstructure and properties of aluminium matrix composite powders. *Mater Sci Eng A*, 342: 131–143.  
[https://doi.org/10.1016/s0921-5093\(02\)00246-0](https://doi.org/10.1016/s0921-5093(02)00246-0)
29. Xu H, Lu Z, Jia C, *et al.*, 2015, Influence of mechanical alloying time on morphology and properties of 15Cr-ODS steel powders. *High Temperature Materials and Processes*, 35: 473–477.  
<https://doi.org/10.1515/htmp-2014-0229>
30. Zhao Q, Yu L, Liu Y, *et al.*, 2015, Morphology and structure evolution of  $Y_2O_3$  nanoparticles in ODS steel powders during mechanical alloying and annealing. *Adv Powder Technol*, 26: 1578–1582.  
<https://doi.org/10.1016/j.appt.2015.08.017>
31. Rahmanifard R, Farhangi H, Novinrooz AJ, 2010, Optimization of mechanical alloying parameters in 12YWT ferritic steel nanocomposite. *Mater Sci Eng A*, 527: 6853–6857.  
<https://doi.org/10.1016/j.msea.2010.07.048>
32. Si C, Zhang Z, Zhang Q, *et al.*, 2021, Influence of mechanical alloying on the particle size, microstructure and soft magnetic properties of coarse Fe-based amorphous powders prepared by gas atomization. *J Non Cryst Solids*, 559: 120675.  
<https://doi.org/10.1016/j.jnoncrysol.2021.120675>
33. AlMangour B, Grzesiak D, Yang JM, 2016, Rapid fabrication of bulk-form  $TiB_2/316L$  stainless steel nanocomposites with novel reinforcement architecture and improved performance by selective laser melting. *J Alloys Comp*, 680: 480–493.  
<https://doi.org/10.1016/j.jallcom.2016.04.156>
34. Sarma IK, Srinivas V, Subbu SK, 2021, Effect of process parameters on micro hardness, bulk hardness and porosity of LENS<sup>TM</sup> deposited SS 316L alloy. *Mater Today Proc*, 46:2616–2624.  
<https://doi.org/10.1016/j.matpr.2021.02.268>